Supplement of Atmos. Chem. Phys., 25, 12721–12735, 2025
https://doi.org/10.5194/acp-25-12721-2025-supplement

Atmospheric Chemistry and Physics
Open Access

Supplement of

Hydroxymethanesulfonate (HMS) formation in urban and marine atmospheres: role of aerosol ionic strength

Rongshuang Xu et al.

Correspondence to: Yan-Lin Zhang (dryanlinzhang@outlook.com, zhangyanlin@nuist.edu.cn)

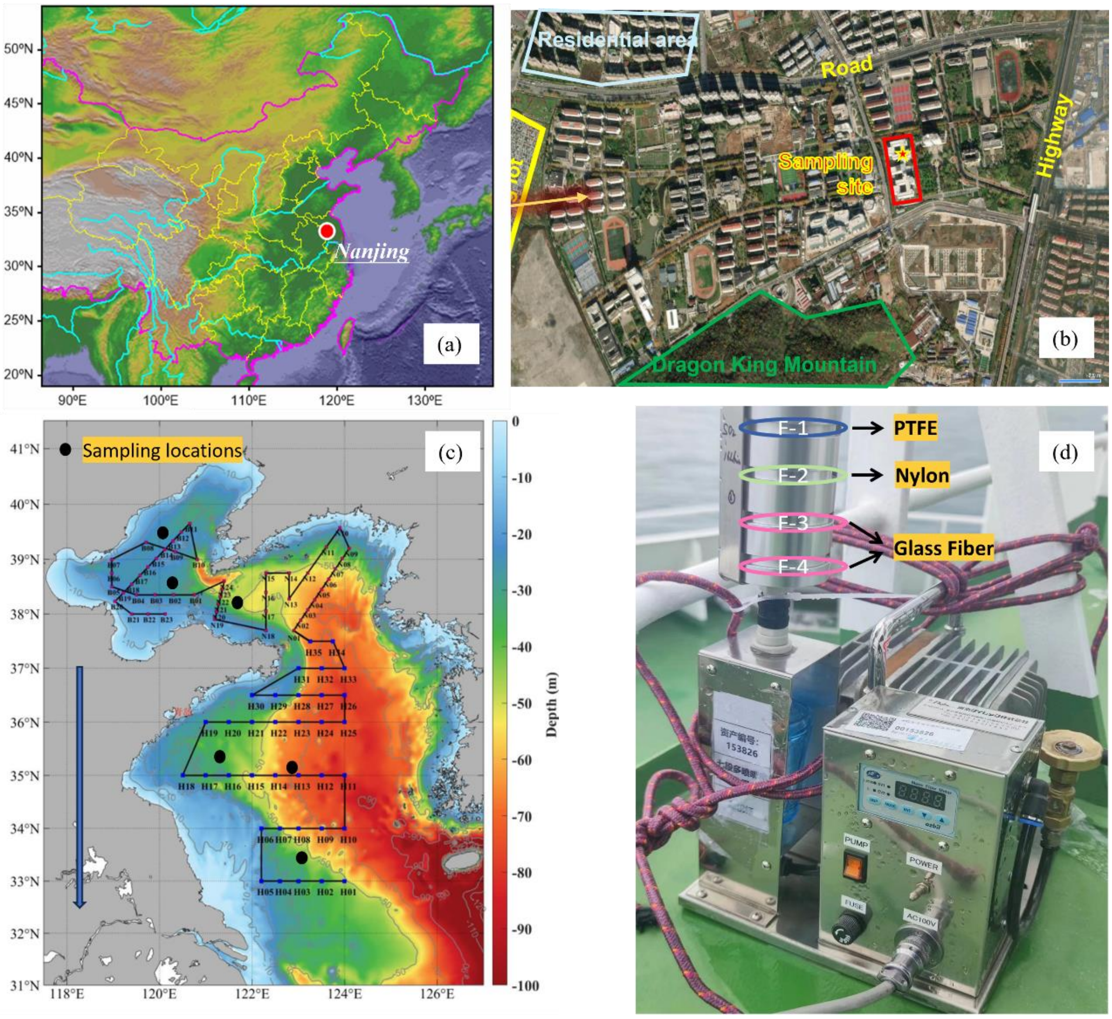

Figure S1. (a) the location of urban aerosols sampling site (Nanjing, China); (b) the surrounding environments of sampling sites located in NUIST campus (base map from © Google Earth); (c) The solid lines in black represent the departing route of the cruise, with the arrow representing the cruise direction. The black dots represent the approximate sampling area for PM$_{2.5}$ and gas-phase SO$_2$ during the cruise with detailed sites shown in **Table S2**; (d) the setup of MCI for offline gas-phase SO$_2$ collection.

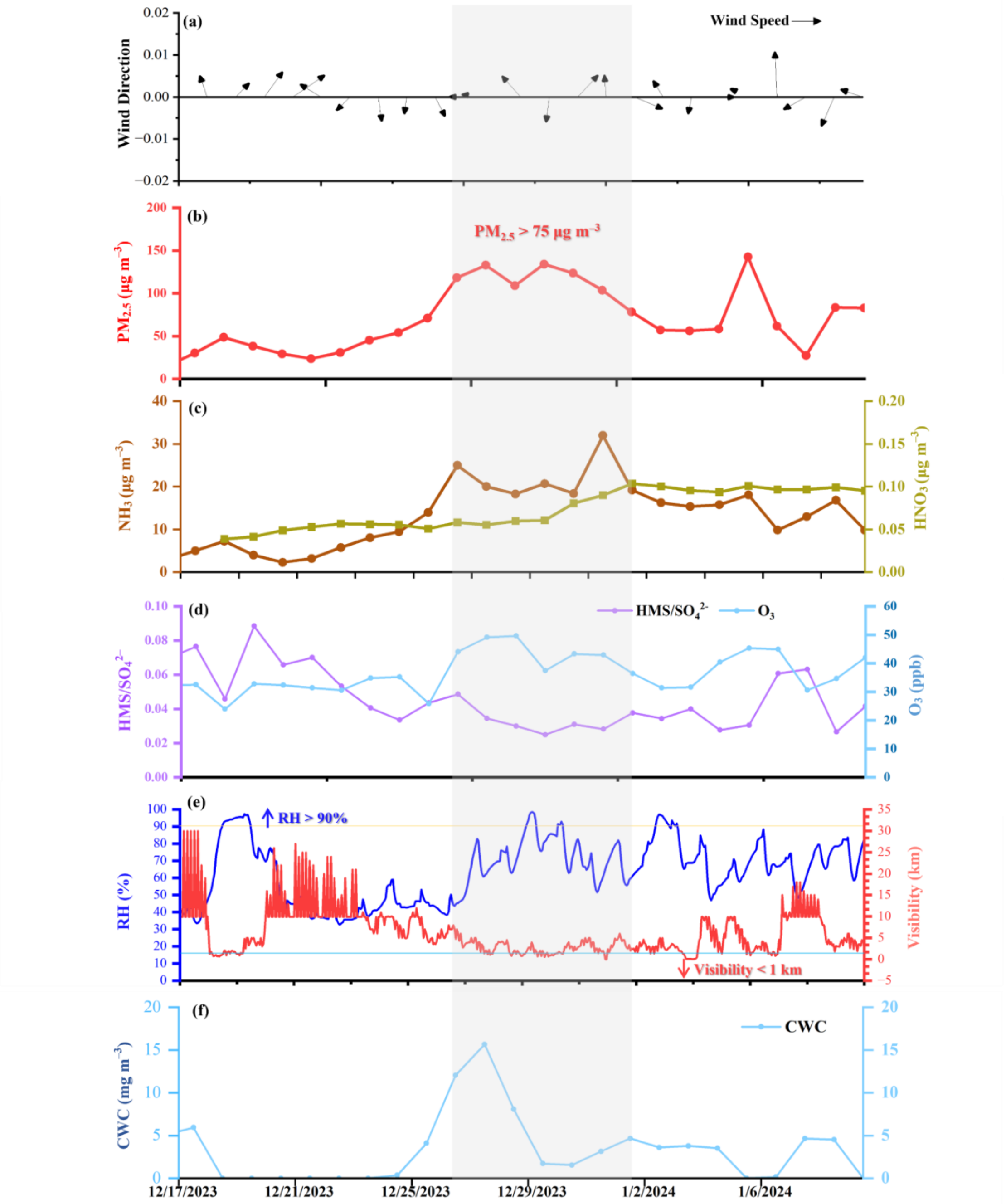

Figure S2. Ancillary atmospheric measurements in urban Nanjing including wind speed and wind direction (a); $PM_{2.5}$ mass concentration (b); gas-phase NH_3 and HNO_3 level (c); O_3 and HMS/SO_4^{2-} ratio (d) and fog event criteria based on hourly relative humidity (RH>90%) and Visibility (<1 km) data (e); Time series of the average cloud water content below the planetary boundary layer height over our observation sites (f).

10

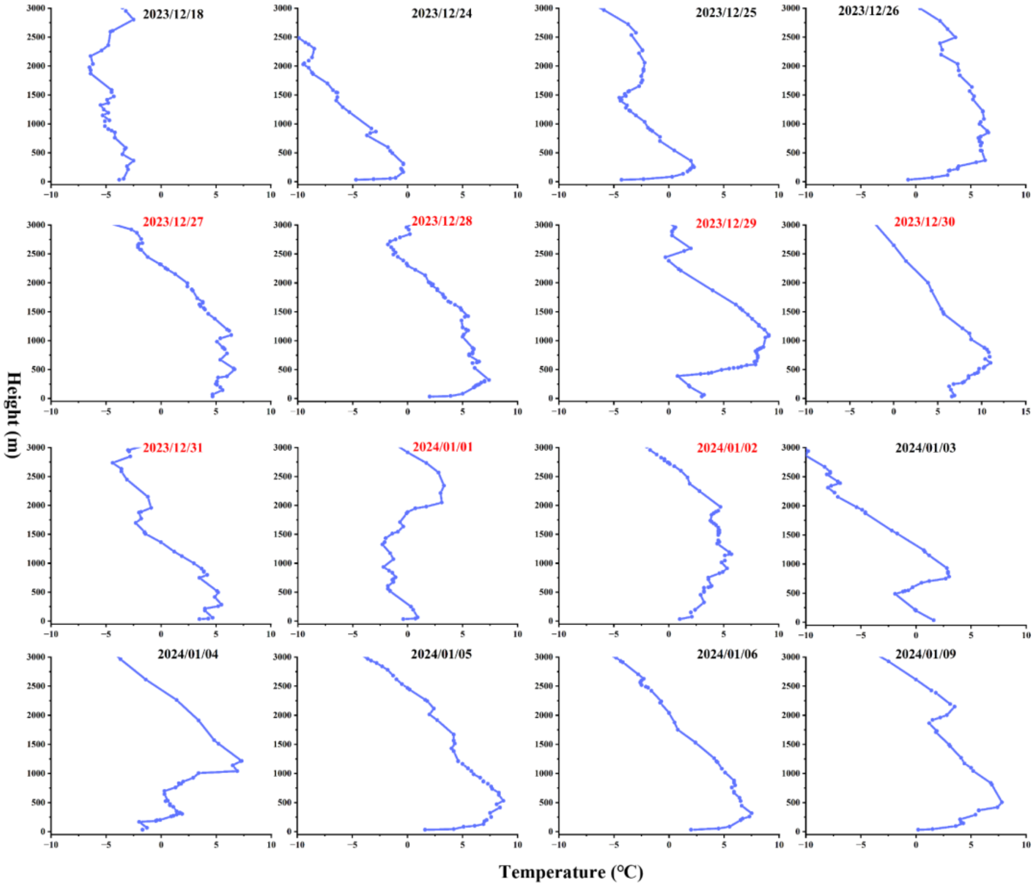

Figure S3. Observed vertical temperature profile at 00 UTC during our observation in Nanjing. The dates of hazy days were marked by red.

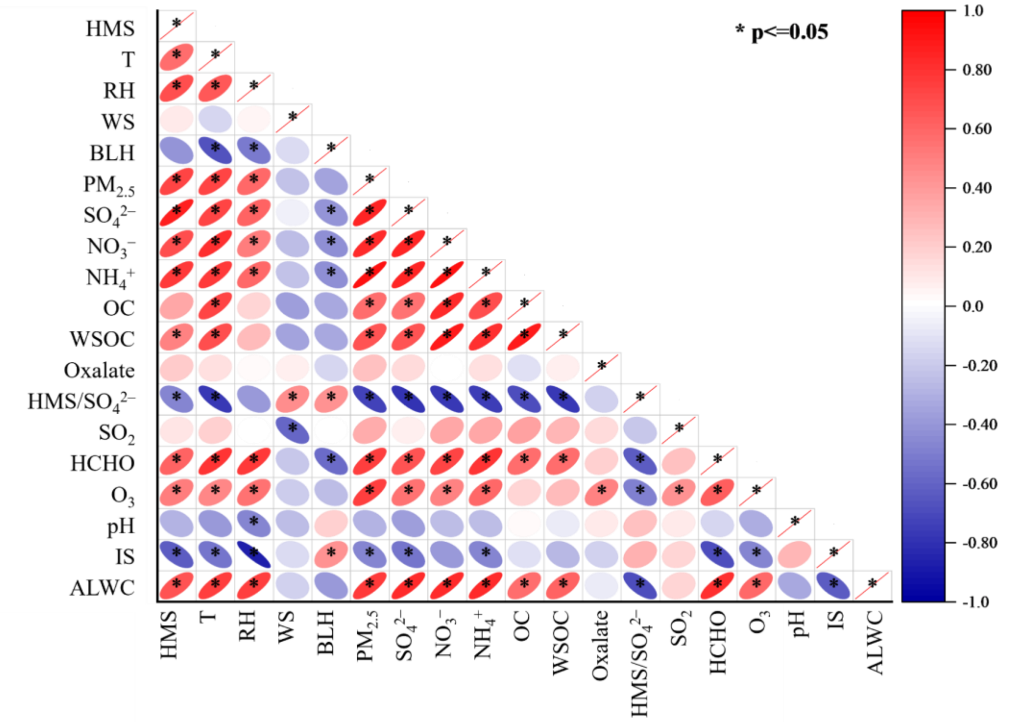

Figure S4. Correlation between HMS concentration and potential influencers in urban Nanjing.

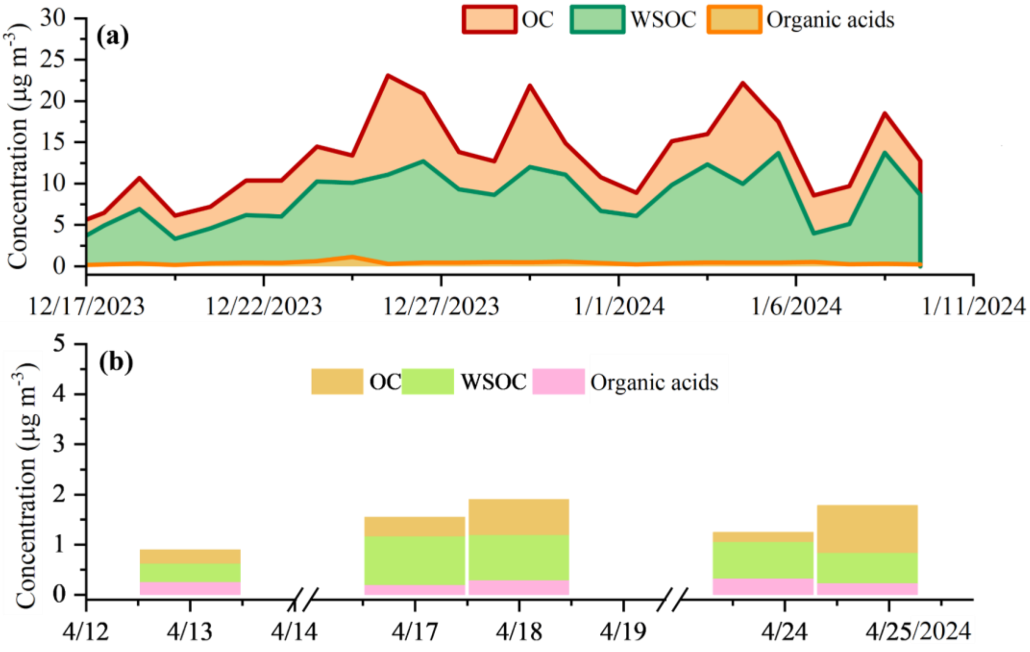

Figure S5. The particulate concentration of OC, WSOC and organic acids observed in urban (a) and marine atmosphere (b). Here the level of OC and WSOC was represented in the unit of C μg m^{-3}, while the unit for organic acids measured by IC was μg m^{-3}.

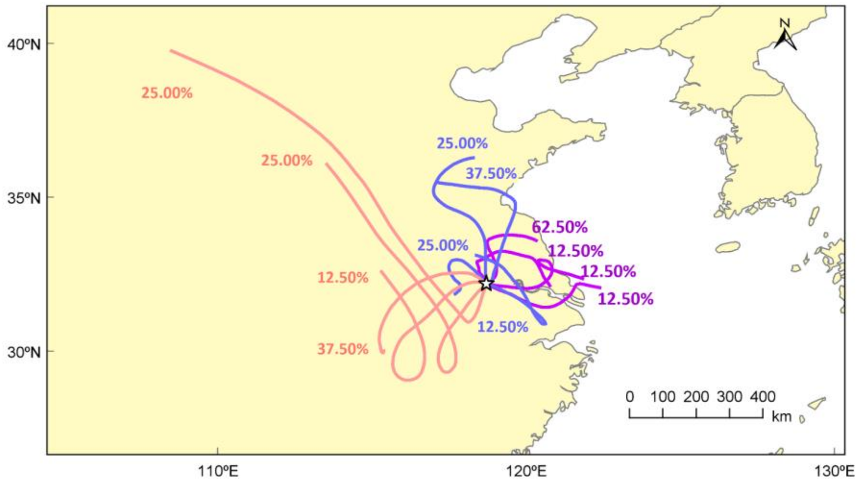

Figure S6. Cluster analysis of backward trajectory at the receptor site in urban Nanjing. The blue, purple, and yellow colors represent the periods of before haze days (December 21st − December 24th, 2023), severe haze episode (December 30th, 2023− January 1st, 2024), and after haze days (January 7−9th, 2024), respectively.

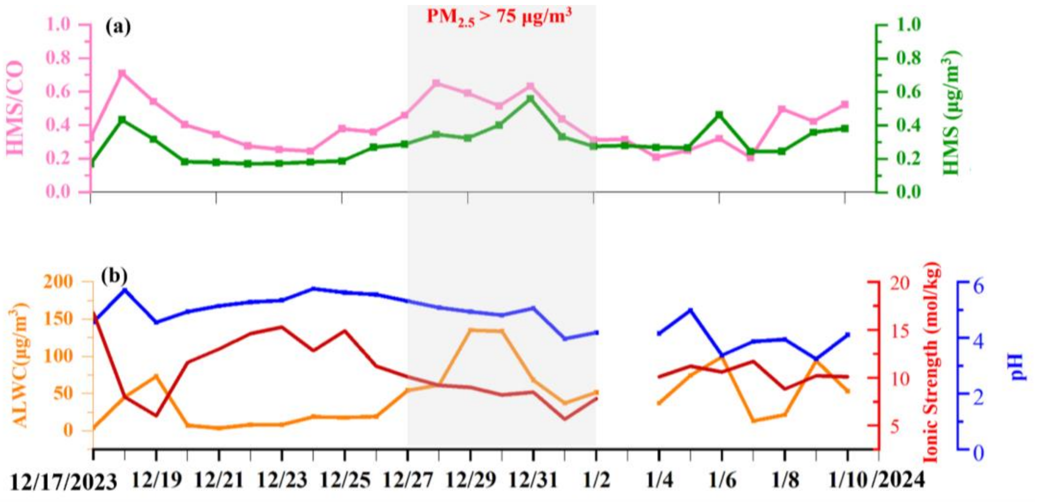

Figure S7. Time series of HMS level and HMS/CO ratio (a), and aerosol properties observed in urban Nanjing (b). The estimation on January 3rd was not available due to the lack of gaseous HNO_3, NH_3, HCl data.

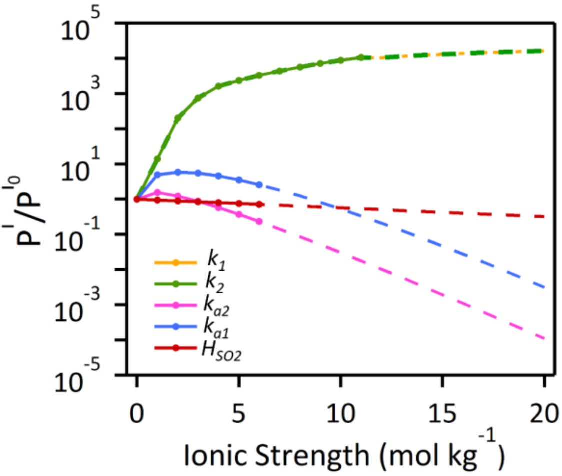

Figure S8. Effects of ionic strength on the Henry's law constant of SO$_2$ (H_{SO2}), the dissociation equilibrium constants of SO$_2$·H$_2$O (k_{a1}, k_{a2}), aqueous reaction rate constants for **R1** and **R2** (k_1, k_2) as determined by the equations listed in **Table S3**. The parameter p^i represents the reaction rate constant or equilibrium constants (p^{i0} refers to the parameter obtained from dilute solution with IS < 1 mol kg^{-1}). Dashed lines indicate extrapolated results based on relationships established from laboratory measured results (**Table S3**).

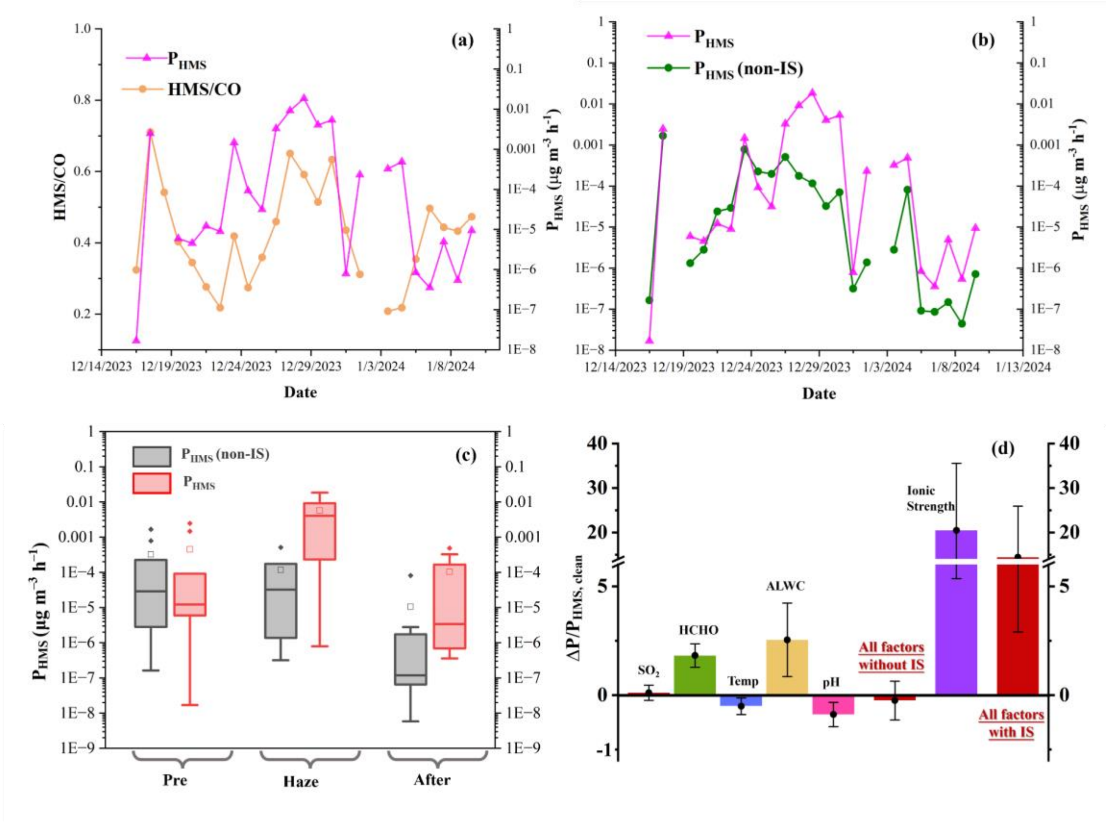

Figure S9. (a) The comparison between estimated HMS formation rate (P_{HMS}) with HMS/CO ratio in urban Nanjing; (b) The comparison between HMS/CO ratio and P_{HMS} without considering the IS effect in urban Nanjing; (c) the averaged P_{HMS} before, within and after haze event, with and without consideration of ionic strength. The formation rate estimations on December 19th, 2023 and January 3rd, 2024 are not feasible due to the absence of HCHO level and aerosol properties, respectively; (d) The relative variation in HMS formation rate during hazy days ($\Delta P/P_{HMS,\ clean}$) corresponding to changes in SO_2 level, HCHO level, temperature, ALWC, pH and ionic strength compared to clean days.

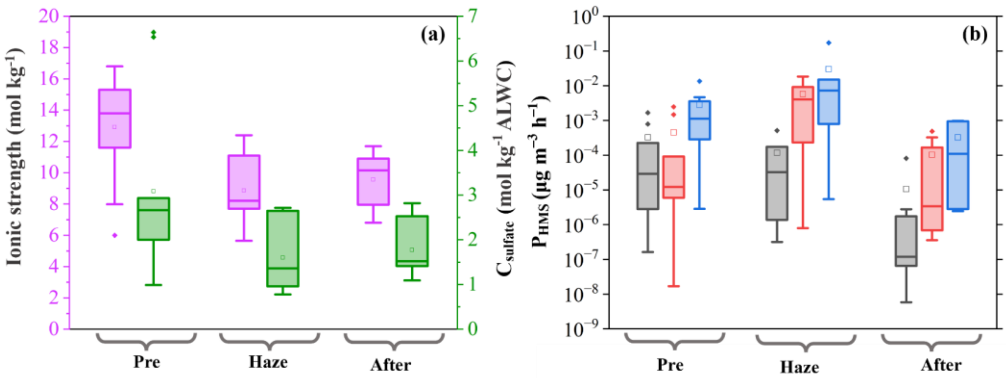

Figure S10. (a) The ionic strength (purple bar) and aqueous sulfate concentration (green bar) in urban aerosols. (b) The P_{HMS} estimations: without the consideration of ionic strength effect and HCHO solubility enhancement (gray bar); with the consideration of ionic strength (pink bar); with the consideration of ionic strength effect and HCHO solubility enhancement (blue bar).

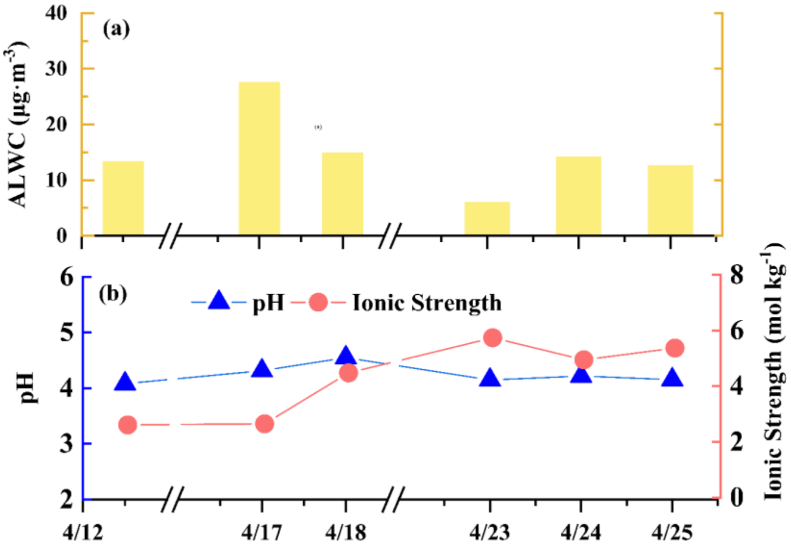

Figure S11. Estimated aerosol liquid water content, pH and ionic strength for marine aerosols.

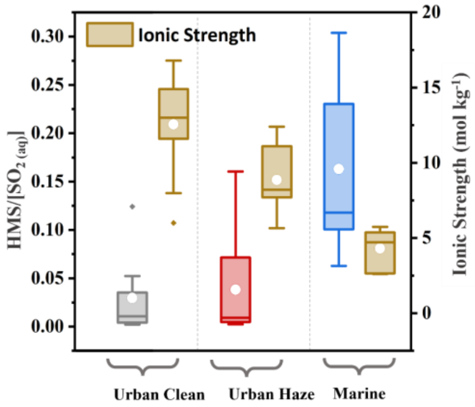

Figure S12. The aqueous conversion ratio for HMS from $SO_{2(aq)}$ (HMS/[$SO_{2(aq)}$]) under diverse atmospheric conditions and aerosol ionic strength level (brown bar).

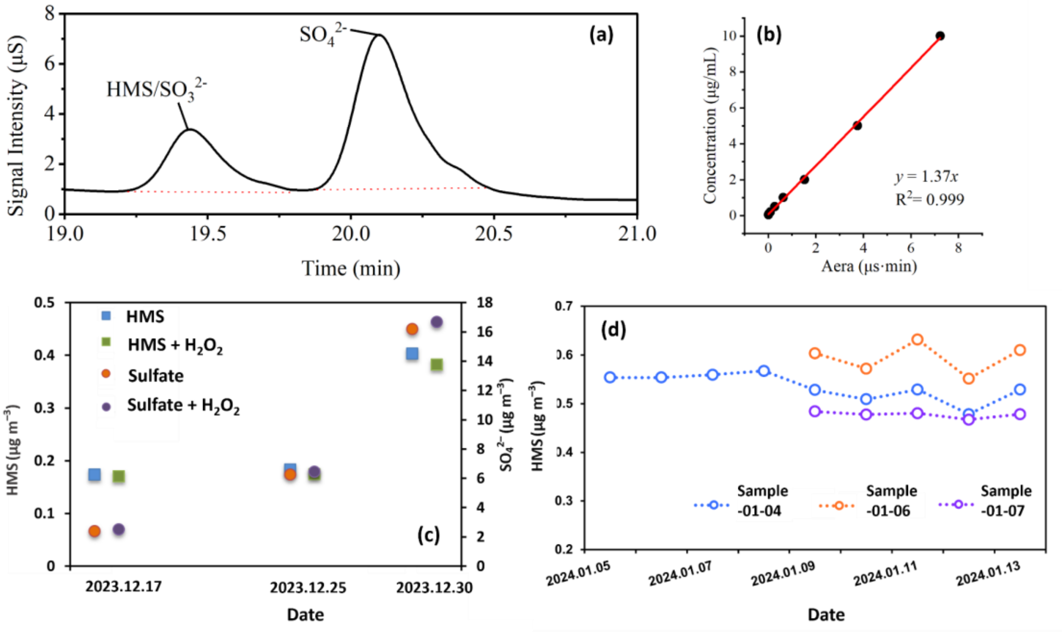

Figure S13. (a) The example ion chromatogram of HMS (sulfite) and sulfate; (b) the calibration curve for HMS quantification; (c) Determination of the impacts from other S(IV) species on HMS/sulfate quantification by adding H_2O_2, which can oxidize the sulfite or bisulfite ions but not HMS; (d) the storage test for HMS stability in quartz membrane filters collected on January 4th, 6th and 7th, 2024.

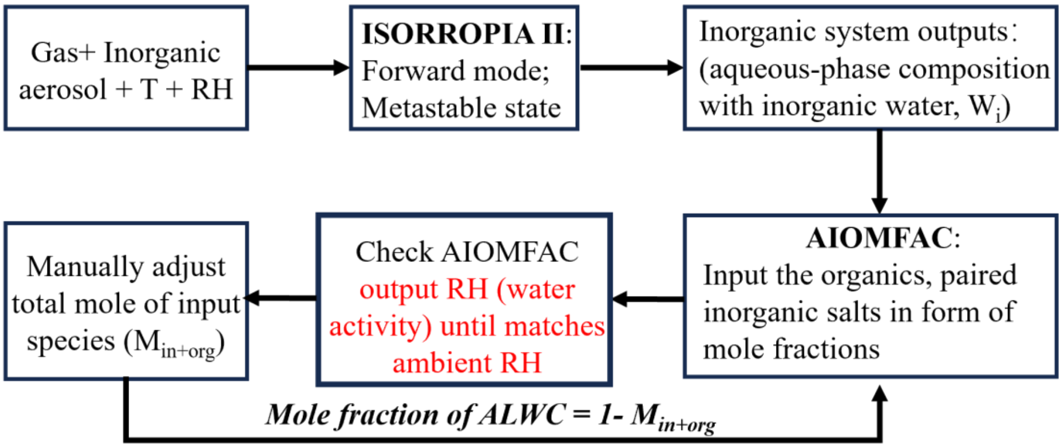

Figure S14. Flow diagram for incorporating ISORROPIA and AIOMFAC to estimate the aerosol properties with consideration of organics. Total moles faction of the organic–inorganic mixed system inputs were adjusted but keep their relative ratio constant until the AIOMFAC-output RH was within 1% of the ambient RH level. Given that the difference between the total inputs and unity was contributed by aerosol water, the aerosol liquid water content together with aerosol pH and ionic strength can be determined according to **Eqn. S2** and **Eqn. S3**.

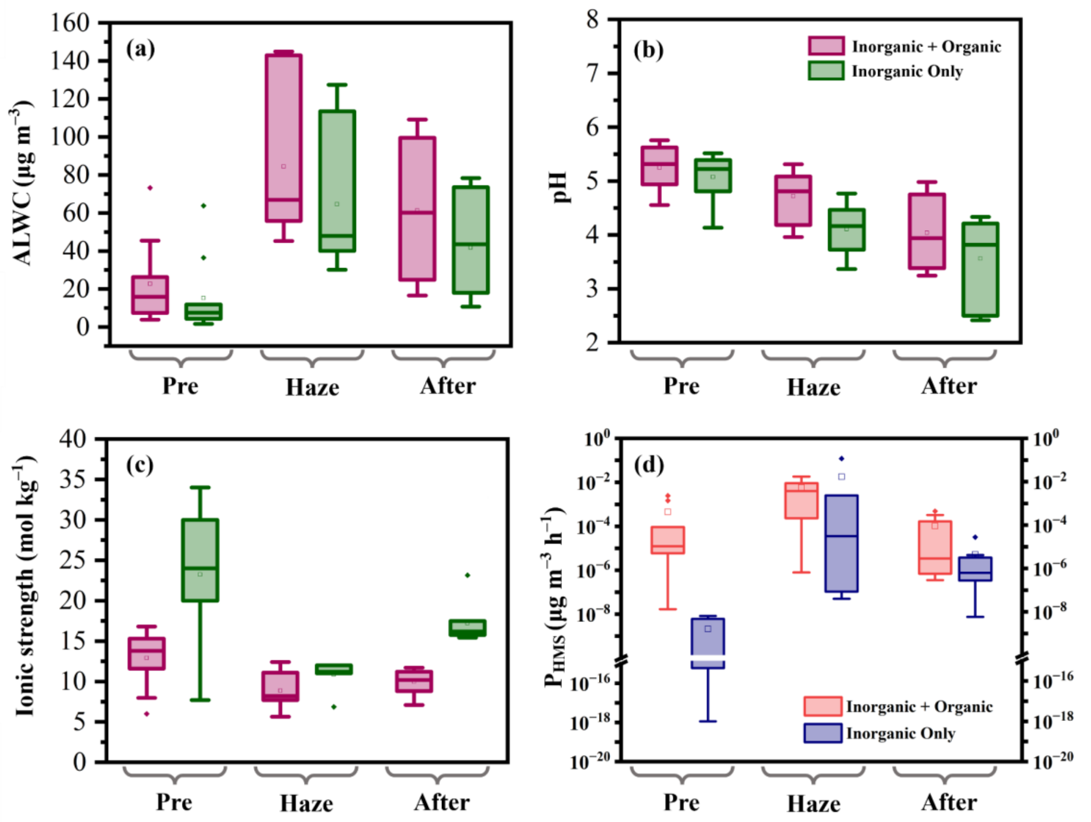

Figure S15. The comparison between estimated aerosol properties (a-c) and P_{HMS} (d) with and without the consideration of organic aerosols, including (a) aerosol liquid water content (ALWC); (b) aerosol pH; (c) aerosol ionic strength.

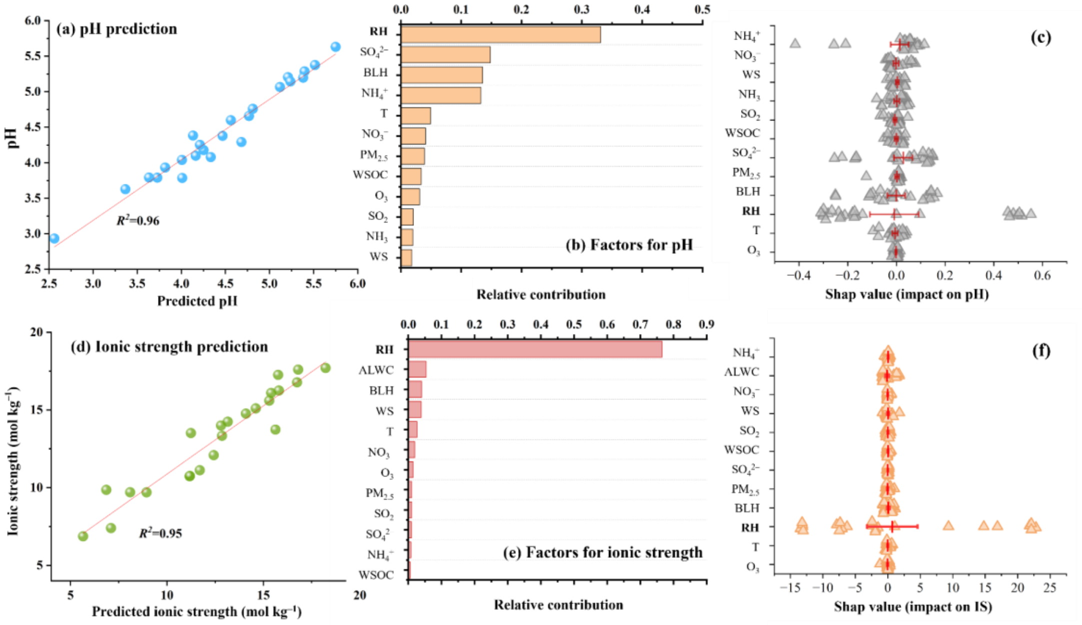

Figure S16. Performance of the Random Forest (RF) model for predicting aerosol pH (a) ionic strength (d); the relative importance of each factor for aerosol pH (b) and ionic strength (e); the Shap (Shapley additive explanations) value of each feature variable on aerosol pH (c) ionic strength (f). T: Temperature; WS: Weed Speed; BLH: boundary layer height.

Section S1. Collection and Chemical Analysis of Ambient Samples

a). Samples Collection

The urban aerosol sampler was installed on the rooftop of Wendelou building within the campus of Nanjing University of Information Science and Technology (NUIST) (32.207°N, 118.717°E). The sampling site was surrounded by roads and residential areas (**Figure S1**). A high-volume $PM_{2.5}$ sampler (Tisch-$PM_{2.5}$, USA) was used to collect $PM_{2.5}$ samples with a flow rate of 1.1 m^3 min^{-1}. Each aerosol sample was collected for 23 hours, i.e., from 8 a.m. to 7 a.m. on the next day. Meteorological data (wind speed and direction, temperature, RH, visibility) were obtained from an automatic meteorological station next to the sampling site. Concentrations of pollutants ($PM_{2.5}$, NO, NO_2, O_3, CO, and SO_2) were obtained from the environmental supervising station at Pukou District, Nanjing, ~15 km away from the sampling site.

$PM_{2.5}$ sampler (Tisch-$PM_{2.5}$, USA) was also equipped onboard of R/V 'Lanhai 101' implementing the open research cruise NORC2024-01 supported by NSFC Shiptime Sharing Project to collect $PM_{2.5}$ samples per day. The sampling locations along the cruise track were shown in **Figure S1**. This sampler was installed windward on the upper deck of the ship, approximately 10 m above the sea surface. The sampler was only turned on when the boat was driving to avoid the pollution of fuel emissions from the hull. A total of 13 samples including 2 blank samples were collected and the onboard monitoring system recorded real-time meteorological information, such as ship travel direction, ambient temperature, humidity, and wind speed (**Figure 1**). It is noted that due to the sampler malfunction and sampling abort coinciding with the halting of the boat and adverse weather conditions, the daily sampling durations exhibited variability, deviating from the intended 23-hour period (**Table S2**). Blank filters (n=2) were collected without airflow during the sampling period. Before sampling, all the quartz filters (size: 8×10 in, PALL USA) were pre-heated in an oven at 450 °C for 6 h to remove impurities in the filters. After sampling, the filters were placed in clean tin foils and stored in the refrigerator (-20 °C) for chemical analysis. In addition, daily gas-phase SO_2 were simultaneously collected using a Multi-Nozzle Cascade Sampler (MCI) with airflow of 4 L min^{-1}. As shown in **Figure S1**, four layers of filters were quipped insider this sampler: the first layer (F-1) was the PTFE filter (47mm, 0.22 μm, PALL) to intercept particulate matters, the second (F-2) one was nylon filter soaked in 1% NaCl solution and 2% glycerol to uptake gas-phase sulfuric acid, the last two layer (F-3, F-4) were glass fiber filters (GF/A-Whatman) to absorb gas-phase SO_2. These glass fiber filters were soaked in the solution of 2% K_2CO_3 and 2% glycerol and dried in an electric oven to ensure SO_2 absorption, which transformed the absorbed SO_2 into SO_3^{2-} and HSO_3^{-}(Guo et al., 2019; Feng et al., 2023). Here, the amount of SO_2 collected by these two SO_2-absorption filters (F-3, F-4) were used to calculate the collection efficiency (CE).

$$CE = (c_1 - c_0)/(c_1 + c_2 - 2c_0) \quad \textbf{(Eqn. S1)}$$

where c_0 is the SO_2 amount collected by blank filters, c_1, c_2 is the SO_2 amount collected by absorption filters F-3 and F-4, respectively. After sampling, the filters were stored in the refrigerator (−20°C) until analysis.

b). Chemical Analysis

To determine the anion and cation concentrations of filter samples, a 16 mm punch of each filter was cut and extracted using 10 mL of Millipore water (18.2 MΩ). Then, the solution was sonicated for 30 min to ensure all of the soluble ions were completely dissolved. Subsequently, part of the filtered extract (0.22 μm, Acrodisc syringe filters) was analyzed using an ion chromatograph (ICS-5000+, Thermo, USA) for quantifying HMS together with other anions (i.e., SO_4^{2-}, NO_3^-, Cl^-, F^-, Oxalate) based on eight-point calibration curves (0.05 to 10 ppm) of multi-element anion standard solutions. During the chromatographic analysis, the eluent was KOH solution, with a flow rate of 1.5 mL min^{-1} and an eluent gradient set to be: 0~1min：0.50mM；4~7min: 5.00mM; 18min: 15.00mM; 23~24min: 30.00mM 25~30min: 0.50mM. The operating temperature was maintained at 30°C. In IC analysis, efficient separations between HMS (retention time = 19.41 min) and SO_4^{2-}(retention time = 20.12 min) were accomplished with a chromatographic resolution of 2.1 (**Figure S13a**). The fitted linear calibration curves of HMS ions were shown in **Figure S13b**, the coefficient of determinations were 0.999. The limit of detection (LOD) and limit of quantification (LOQ) were estimated based on replicates of low concentration samples (i.e., at 0.05 and 0.5 ppm), respectively. Here, the LOD and LOQ for HMS was determined to be 4 ng·mL^{-1} and 20 ng mL^{-1}, respectively. The measurement precision, determined by repeatability tests (n=10) at two calibration points (0.05 ppm and 0.5 ppm), was less than 2%. The LOD, LOQ and precision of other anion and cations (NH_4^+, Ca^{2+}, Na^+, Mg^{2+}, K^+) can be found in our previous study (Fan et al., 2019). It is noted that HMS was detected in the form of sulfite in IC analysis as it can readily decompose into sulfite upon mixing with the alkaline eluent (Wei et al., 2020; Lai et al., 2023). Therefore, free S(IV) (i.e., sulfite and bisulfite) or other S(IV) species such as aldehyde-S(IV) adducts may be misidentified as HMS during the IC analysis (Ma et al., 2020; Dingilian et al., 2024). Thus, to determine the potential error in HMS quantification raising from free S(IV) and aldehyde-S(IV) adducts, 0.1 mL of 3% H_2O_2 was added into the second aliquot of the closed sample extracts, which converted other S(IV) species to sulfate over a reaction period of 3 hours (Dingilian et al., 2024). Before injected into IC, 0.1 mL volume of H_2O_2 catalase solution (>200.000 unit/g, Aladdin) was added to destroy any excess H_2O_2. As shown in **Figure S13c**, here we tested 3 samples and found that the deviations in HMS quantification resulted from other S(IV) species were less than 5%, consistent with previous findings (Wei et al., 2020). Considering that HMS is quite stable under acidic conditions (pH<6) but become unstable under alkaline environments and dissociates rapidly into SO_3^{2-} and HCHO (Seinfeld and Pandis, 2016), here we also tested the pH of filter aliquots of two hazy days (December 28th and 31st, 2023) and one clean day (December 24th, 2024) using a pH-meter (Sartorius, PB-10). The determined pH values were 5.68, 5.71, and 5.79, respectively, all falling below the threshold of 6. And half of these aliquots were immediately injected to IC and the other half was injected after 3 hours. The results shown there was less than 5% of difference in HMS level between these IC analyses. Besides, prior study has pointed out the decomposition of HMS in quartz membrane filters over long-term storage (i.e., 4 months) (Moch et al., 2018; Moch et al., 2020). Here we also tracked the changing of HMS concentrations in filters over a 2-weeks storage periods and the results suggested the HMS were likely remain stable with standard deviation less than 2%. Thus, we believed the decay of HMS was negligible during the interval (<2 weeks) between sample collection and our chemical analysis. Extracts from SO_2-absorption filters were also injected into IC to determine the daily averaged gas-phase SO_2 concentration.

For determination of OC and EC concentrations, a portion of each quartz filter was examined using a sunset OC/EC analyzer (Sunset Laboratory Inc.), and the samples were processed according to the IMPROVE (Interagency Monitoring of Protected Visual Environments) thermal desorption and optical reflectance method with a 550 °C temperature, split for OC and EC (Chow et al., 2007). For determination of WSOC concentrations, a portion of each quartz fiber was extracted with 10 mL of ultrapure water for 30 min at room temperature. The water extracts were passed through a polyvinylidene difluoride filter (0.22 µm, Acrodisc syringe filters) to remove insoluble materials, and then the filtrate was analyzed using a total organic carbon analyzer (TOC-L, Shimadzu, Kyoto, Japan).

Section S2. HCHO Concentration Retrieval from MAX-DOAS

In this work, the surface HCHO concentration was retrieved based on multi-axis differential optical absorption spectroscopy (MAX-DOAS) measurements operated near our sampling site in Nanjing. Detailed descriptions regarding the instruments set-up, operation procedure, and data acquisition can be found in our previous studies (Xing et al., 2017; Xing et al., 2021; Hong et al., 2022a; Liu et al., 2022). Briefly, measured scattered sunlight spectra from MAX-DOAS were analyzed for the differential slant column densities (DSCDs) of HCHO, which was used as input parameters to retrieve vertical profiles of HCHO through USTC algorithm (Xing et al., 2017) based on optimal estimation method (OEM) (Rodgers, 2000) and used a radiative transfer model linearized pseudo-spherical vector discrete ordinate radiative transfer models (VLIDORT) (Spurr, 2006) as the forward model (Liu et al., 2022). The concentrations of HCHO were presented by the maximum a posteriori state vector *x* from following cost function:

$$\chi^2 = \big(y - F(x,b)\big)^T S_\varepsilon^{-1}\big(y - F(x,b)\big) + (x - x_a)^T S_a^{-1}(x - x_a)$$

Where y was observed DSCDs; $F(x, b)$ was the forward model results; b was ancillary parameters (i.e., meteorological, aerosol optical properties and surface albedo); x_a was a priori information; S_ε and S_a were the covariance matrices of y and x_a. In this study, we set up the atmosphere to 20 layers from 0 to 3 km. The vertical resolution under 1 km and 1-3 km were 0.1 km and 0.2 km, respectively. The HCHO concentration in the 0–100 m layer was used as the ground-level HCHO level. The uncertainty of HCHO profiles retrieved using above algorithm were less than 10% (Xing et al., 2017; Xing et al., 2021; Hong et al., 2022a; Liu et al., 2022).

Section S3. Backward Trajectories Analysis

Hybrid Single-Particle Lagrangian Integrated Trajectory (HYSPLIT) was used to analyze the air masses before, during and following the $PM_{2.5}$ pollution period. The details of the FLEXPART model can be found elsewhere (Han et al., 2022). Meteorological data used here were obtained from the Global Data Assimilation System (GDAS) with a 1°×1° spatial resolution and 3-h temporal resolution. The 72-h backward trajectories at a height of 100 m obtained from the National Oceanic and Atmospheric Administration were run every hour. Cluster analysis was performed using Meteoinfomap, and four clusters were determined based on the total spatial variance (TSV) (Wu et al., 2023). As shown in **Figure S5**, the backward trajectories suggested that the air masses before and during the haze episode were predominantly originated from the vicinity, whereas nearly half of the air masses following the hazy days were transported over long distances from the northwest. Hence, the emergence of this haze episode likely stemmed from local sources, with the heightened levels of HMS probably being formed on-site rather than transported from other locations.

Section S4. Aerosol Properties Estimations

In this study, we integrated the ISORROPIA II and Aerosol Inorganic-Organic Mixtures Functional groups Activity Coefficient (AIOMFAC) model to estimate aerosol liquid water content (ALWC), pH, and ionic strength (IS), following the methodology outlined by previous work (Battaglia et al., 2019). A flow diagram of this combined method was given in **Figure S14**. For urban aerosols, inorganic PM composition (SO_4^{2-}, NO_3^-, Cl^-, Na^+, NH_4^+, Ca^{2+}, K^+ and Mg^{2+}) and gaseous HNO_3, NH_3, HCl data obtained by MARGA together with temperature (T) and relative humidity (RH), were input into ISORROPI II under "Forward" mode and "metastable" state, aiming to derive equilibrium concentrations of aerosol liquid water content (ALWC) and all ionic species present under specified T and RH conditions. For marine aerosols, as the gaseous NH_3 measurements were not available during sampling period, we assumed a total NH_x (= NH_3 + NH_4^+) as factor of two times measured NH_4^+, corresponding to a particle to particle + gas partitioning fraction of NH_4^+ (ε) of 0.5. And the gas-phase contributions of HNO_3 and HCl to total nitrate (nitric acid) and chloride was not considered here given the fact that partitioning of these acidic gases was expected to be exclusively in the particle phase considering the pHs range for freshly emitted sea spray aerosol (pH>7) and even acidified particles (4-6) (Campbell et al., 2022). Subsequently, organic components in conjunction with the inorganic matrix outputs from ISORROPIA II were incorporated into AIOMFAC model at the same T. During AIOMFAC run, it was required the inorganic species inputs entered as ionic pairs to ensure electroneutrality. As suggested by Battaglia et al. (2019), the ionic pairs were assigned in the following ways. First, all SO_4^{2-} was paired with H^+ for the H_2SO_4 pair in AIOMFAC. All NO_3^- was associated with Na^+ for the $NaNO_3$ pair. The remaining Na^+ was associated with SO_4^{2-}, then NH_4^+ with HSO_4^-, and the remaining NH_4^+ with the remaining SO_4^{2-}. The ion-pairing scheme was unlikely to affect model outcomes as all the matched cation–anion pairs were expected to be fully dissociated in the aqueous phase during AIOMFAC model simulation. When introducing the organics into AIOMFAC, all species (both inorganic and organic) needed to be inputted in mole or mass fractions. The model then assumed that water made up the difference between the sum of mole or mass fractions of all organic and inorganic inputs and unity, with the water activity (a_w) equating to the ambient relative humidity (RH). Then, the total moles of inputs were adjusted manually while maintaining the relative ratios between each species constant until the RH values predicted by AIOMFAC were within 1% error of the RH value set for the ISORROPIA II model. The output aerosol compositions from AIOMFAC were used to predict aerosol properties such as ALWC, pH, and ionic strength (IS) using the following equations:

$$\mathrm{pH} = -\log_{10}(\gamma_{H^+} m_{H^+}) \quad \textbf{(Eqn. S2)}$$

$$\mathrm{IS} = 1/2 \sum m_i z_i^2 \quad \textbf{(Eqn. S3)}$$

where the γ_{H^+} and m_{H^+} was the AIMOFAC outputted molality-based activity coefficient and molality of H^+, respectively. The m_i and z_i represented the molality of each ion and its corresponding charge.

In this study, the mole or mass contribution of organics was calculated based on the measured WSOC mass concentration. Considering the typical hygroscopicity (k) ranging from 0.1 to 0.2 and the composition of organic aerosols (Liu et al., 2021a; Pöhlker et al., 2023), levoglucosan ($C_6H_{10}O_5$, k=0.16±0.01) (Petters and Kreidenweis, 2007) were selected as model organic species found in ambient aerosols. Recognizing the potential influence of organic acids on aerosol properties through mechanisms such as increased water uptake and the provision of free H^+ ions and ionic concentrations, the low concentrations of organic acids identified in this study (**Figure S4**) suggested that their impact on aerosol properties was likely to be minimal. It was important to recognize that the model outputs may not completely represent the hygroscopic nature of organic aerosols because of incomplete information concerning the speciation and concentrations of organic components. Furthermore, the model did not account for the re-equilibration of gas-phase species with the altered water content caused by the organic species through AIOMFAC, leading to estimation bias in ALWC.

The model output results and its comparison with inorganic-only simulations from ISORROPIA II for urban aerosols was shown in **Figure S15**. Briefly, there was consistent patterns in aerosol properties variations across different pollution conditions regardless of the inclusion of organic aerosols with higher ALWC and lower pH and ionic strength estimations for humid and polluted days. When organic components were considered, ALWC values were estimated to be approximately 20±8% higher during hazy days and 48±10% higher on clean days compared to inorganic-only estimations. The more significant variance on clean days was attributed to a greater contribution of water-soluble organics to $PM_{2.5}$ (20±14%) compared to hazy days (10±2%). Additionally, the inclusion of organics led to slightly elevated aerosol pH values (ΔpH $\leq$ 0.5 unit), in line with prior research (Battaglia et al., 2019). This slight pH increase can be attributed to non-dissociating organic compounds in aerosols enhancing water absorption and subsequently reducing H^+ concentration. These minor deviations hint at the predominant influence of inorganic constituents on aerosol pH levels. With the consideration of organics, this work estimated lower ionic strengths during our observation in Nanjing, with more substantial reduction observed on dry and clean days (48±33%) compared to humid and polluted period (25±17%). The pronounced differences in ionic strength estimations under dry and clean conditions can be partially explained by the increase in ALWC (up to 50%), driven by the hygroscopic nature of organic species. This rise in ALWC resulted in significant dilution of the aerosol solution, leading to reduced concentrations of ionic species. A previous study utilizing ISORROPIA II also noted higher ionic strength under low humidity conditions that the ionic strength could exceed 60 mol kg^{-1} under 40% RH and drop sharply to less than 10 mol kg^{-1} when RH increased over 80% with constant aerosol composition (Song et al., 2018). Besides, a measurement-based study reported a much narrower range of ionic strength for urban aerosols in Los Angeles (ranging from 8.0 to 18.6 mol kg^{-1}) based on measured ionic concentration and aerosol water mass content (Stelson and Seinfeld, 1981) where aerosol mass concentration ranged from 82 to 192 μg m^{-3} with RH of ~ 55%. These results suggested the important role of organic species in determining aerosol ionic strength, primarily by impacting the aerosol water content. Overall, it was anticipated that the inclusion of organic components in thermodynamic models can lead to more precise representations of aerosol properties, particularly under lower humidity conditions. However, it is important to acknowledge potential uncertainties in our estimations, particularly under lower humidity, as ambient aerosols containing water-soluble inorganic and organic components may undergo phase separation, resulting in uneven phase distribution and mixing states. Additionally, we compared the HMS formation rates (P_{HMS}) using the aerosol properties estimation with and without consideration of impact of organics (**Figure S15d**). The results revealed that haze events consistently exhibited higher formation rates compared to clean days, regardless of the inclusion of organics and P_{HMS} for clean days under inorganic-only scenarios were notably lower due to lower ALWC and pH levels, alongside higher ionic strength.

In addition, here we utilized a random forest (RF) model with Shapley additive explanations (SHAP) to identify crucial factors influencing aerosol pH and ionic strength, as widely used in previous studies (Li et al., 2024; Zhang et al., 2025). Details of the specifications of RF model can be found in our previous studies (Hong et al., 2022b; Fan et al., 2023). Briefly, the RF model was fed by trace gases, meteorological parameters, chemical components and aerosol pH/ionic strength. The inputs were randomly divided into a training set (80%) and a test set (20%). Model performance was evaluated using traversal functions with root-mean-squared error (RMSE), mean-absolute error (MAE), and correlation coefficient (R^2) as the evaluation metrics. The contributions of these driving factors were quantified using SHAP values that a larger SHAP value of a feature indicates a higher contribution and the relative importance of various factors can be calculated by the mean of absolute SHAP value. For aerosol pH evaluations, the model input includes T, RH, Weed Speed (WS), boundary layer height (BLH), $PM_{2.5}$, SO_4^{2-}, NO_3^-, NH_4^+, SO_2, O_3, NH_3. It is noted that previous study has point out that RH, as a more general environmental parameter, is more suitable as an input parameter than ALWC for assessing aerosol pH, given the quantitative relationship between pH and ALWC (Zhang et al., 2025). Consequently, ALWC was excluded from the input factors. As shown in **Figure S16a**, the aerosol pH predicted by RF model closely matches our calculation from thermodynamic models, with R^2 of 0.96. And RH has the highest contribution (**Figure S16b**) and largest Shap value (**Figure S16c**) on aerosol pH. Besides, SO_4^{2-} rank as the second most important factors, surpassing the contribution of NO_3^-. This result was in consistent with previous work in NCP region (Ding et al., 2019), which declared that SO_4^{2-} had a greater effect than NO_3^- on $PM_{2.5}$ pH as SO_4^{2-} can lead to a higher concentration of H^+_{air} than NO_3^- due to its low volatility and strong dissociation. To determine the key drivers for ionic strength variations, the model inputs include T, RH, WS, BLH, $PM_{2.5}$, SO_4^{2-}, NO_3^-, NH_4^+, SO_2, O_3 and ALWC. As shown in **Figure S16d**, the aerosol ionic strength predicted by RF model closely matches the outputs of thermodynamic models, with R^2 of 0.95. And RH has the dominant contribution of 76% and largest SHAP value on aerosol ionic strength, following by the ALWC (**Figure S16e-f**). This could be explained by that higher RH levels enable increased water absorption, subsequently elevating ALWC. In the meantime, heightened ALWC can facilitate the formation of inorganic ions through gas-particle conversion and the partitioning of gas pollutants, potentially leading to an accumulation in the aqueous-phase ionic components. These findings align with correlation analyses that demonstrated a stronger correlation between RH and Ionic Strength (IS) (R=-0.89) compared to that between ALWC and IS (R=-0.62, $p<0.05$), underscoring the predominant influence of RH in determining ALWC and IS in our study area.

Section S5. Steady-state HMS formation rate calculation in aqueous aerosols

In the aqueous phase, reactions **R1** and **R2**, initially proposed by Boyce and Hoffmann (Boyce and Hoffmann, 1984), have been extensively employed in model simulations to depict the formation of HMS. A recent laboratory study suggested that HMS can also be formed through the aqueous-phase reaction between SO_2 with glyoxal (De Haan et al., 2020). Given that glyoxal serves as a crucial precursor of oxalate, the strong correlation observed between HMS and oxalate has led to the proposition that the formation of HMS via the glyoxal-SO_2 pathway holds potential importance (Zhang et al., 2024). However, no clear correlation between oxalate and HMS was observed in this study (**Figure 2**). Therefore, it was anticipated that the HMS observed during our sampling period was predominantly formed through the HCHO-SO_2 pathway and the reaction rate can be expressed in the unit of M s^{-1}:

$$\mathrm{R_{HMS}} = \left(k_1 \times [\mathrm{HSO_3^-}] + k_2 \times [\mathrm{SO_3^{2-}}]\right) \times [\mathrm{HCHO_{(aq)}}] \quad \textbf{(Eqn.1)}$$

The aqueous phase reaction inside bulk aerosols or fog droplets required the dissolution of SO_2 and HCHO. The equilibrium of gaseous and its corresponding aqueous species was assumed to follow Henry's law and the concentrations of dissolved $SO_{2(aq)}$ and $HCHO_{(aq)}$ can be determined by:

$$[\mathrm{SO_{2(aq)}}] = H_{SO2} \times P_{SO2}$$

$$[\mathrm{HCHO_{(aq)}}]_t = H_{HCHO} \times P_{HCHO}$$

$$[\mathrm{HCHO_{(aq)}}] = 1/(1+K_h) \times [\mathrm{HCHO_{(aq)}}]_t$$

The H_{SO2} and H_{HCHO} represented the Henry's law constant for SO_2 and HCHO, respectively, which were related to the temperatures. The H_{SO2} was also affected by the ionic strength of aqueous solution as summarized in **Table S3** (Millero et al., 1989). The aqueous-phase concentration of SO_3^{2-} and HSO_3^- was highly dependent on both the solution acidity and ionic strength with relations given in **Table S3**.

$$[\mathrm{HSO_3^-}] = k_{a1} \times [\mathrm{SO_{2(aq)}}] / [\mathrm{H^+}]$$

$$[\mathrm{SO_3^{2-}}] = k_{a2} \times [\mathrm{HSO_3^-}]/[\mathrm{H^+}]$$

After dissolution, HCHO can be hydrolyzed in aqueous solution to yield the gem-diol form $H_2C(OH)_2$ with chemical equilibrium constant, K_h (Winkelman et al., 2002).

The HMS formation rate in bulk aerosol can by determined as follows:

$$\mathrm{P_{HMS}} = \mathrm{R_{HMS}} \times \mathrm{ALWC} \times 3600 \times \mathrm{M_{HMS}} \quad \textbf{(Eqn. 2)}$$

where the $\mathrm{P_{HMS}}$ was expressed as μg m^{-3} h^{-1}, ALWC represented the aerosol liquid water content (μg m^{-3}). In addition, the mass transport process of gas precursors from gas phase to particle phase may also limit the reaction rate, which can be considered using a resistor model (Cheng et al., 2016):

$$\frac{1}{\mathrm{R_{HMS,aq}}} = \frac{1}{\mathrm{R_{HMS}}} + \frac{1}{\mathrm{J_{aq,lim}}} \quad \textbf{(Eqn. S4)}$$

where the $\mathrm{R_{HMS,aq}}$ is overall reaction rates (M s^{-1}), and $\mathrm{J_{aq,lim}}$ is mass transport limiting rate ($\mathrm{J_{aq,lim}} = \min\{\mathrm{J_{aq,SO2}}, \mathrm{J_{aq,HCHO}}\}$).

$$\mathrm{J_{aq,X}} = \mathrm{k_{MT}(X)} \times \mathrm{P(X)} \times \mathrm{H(X)} \textbf{(Eqn.S5)}$$

where X presented SO_2 or HCHO, $P(X)$ was the partial pressure of X (atm) and $H(X)$ was the effective Henry's law constant (mol L^{-1} atm^{-1}), $k_{MT}(X)$ was the mass transfer coefficient of species X in s^{-1}.

$$k_{MT}(X) = \left[\frac{R_P^2}{3D_g} + \frac{4R_p}{3\alpha\nu}\right]^{-1} \quad \mathbf{(Eqn. S6)}$$

where the R_p was the radius of aerosol particles (μm), D_g, α and ν refered to the gas-phase diffusivity (cm^2 s^{-1}), the mass accommodation coefficient (unitless) and mean molecular speed (m s^{-1}) of a given gas species. Here, using 0.15 μm for R_p (Liu et al., 2021b), D_g of 0.1 cm^2 s^{-1}, ν of 300 m $s^{-1}$and α of 0.11 for SO_2 and 0.02 for HCHO (Seinfeld and Pandis, 2016), this mass transfer limitation exerted a negligible impact on the HMS formation rates. This also aligned with previous findings suggesting minimal effects of mass transfer limitations on various multi-phase SO_2 oxidation pathways (Liu et al., 2021b; Yu et al., 2023). Considering the ionic strength effect on the rate constants for **R1** and **R2** (Zhang et al., 2023), here the overall HMS formation rate can be determined as shown in following **Table S3**.

After formation, HMS can undergo further decomposition (**R3**) (Boyce et al., 1984; Dixon and Aasen, 1999) or oxidation (**R4**) (Boyce et al., 1984; Olson and Hoffmann, 1986; Lai et al., 2023) processes. Previous studies have suggested that the HMS is quite stable under acidic conditions but become unstable under alkaline environments and dissociates rapidly into $SO_3{}^{2-}$ and HCHO, with lifetime of a few hours at pH of 6 (Munger et al., 1986) and less than 1 min at pH of 9 (Seinfeld and Pandis, 2016). Considering the aerosol pH range observed in this study, the chemical sink of HMS via **R3** was expected to be insignificant. Besides, although HMS is resistant to the oxidation of H_2O_2 and O_3, it can be oxidized by •OH radicals within aqueous solution and/or at the aerosol surface. However, a recent model study suggested that this process only led to a less than 10% reduction in HMS abundance in winter season (Wang et al., 2024). Therefore, here we proposed that these chemical removal processes of HMS may play a negligible role in governing its ambient concentrations.

$$HOCH_2SO_3^- + OH^- \rightarrow SO_3^{2-} + HCHO_{(aq)} \quad \mathbf{(R3)}$$

$$HOCH_2SO_3^- + \bullet OH + O_2 \rightarrow SO_4^{2-} + HCHO_{(aq)} \quad \mathbf{(R4)}$$

Section S6. Aqueous HMS conversion ratio calculation in aerosol water

The aqueous HMS conversion ratio (R^a) can be calculated using following equation:

$$R^a = \frac{[HMS]/M}{H_{SO2}^{*} \times P_{SO2} \times ALWC/\rho_{water}} \times 10^6 \quad \mathbf{(Eqn. S7)}$$

where the [HMS] (μg m^{-3}) was the ambient level of HMS, M (g mol^{-1}) was the molar mass of HMS, P_{SO2}(ppb) was the gas-phase SO_2 level, H_{SO2}^{*} was the effective Henry's law of SO_2 with the consideration of aqueous solution pH and ambient temperature, ALWC (μg m^{-3}) was the aerosol water content, and ρ_{water} was the water density.

Table S1. Summary of atmospheric measurements in this study.

	Continental aerosol			Marine aerosol
	Pre-haze	**Haze event**	**After haze**	
T (K)	272±2 [a]	277±4	277±1	283±1
RH	52±17%	74±8%	69±5%	83±6%
$PM_{2.5}$ (μg m^{-3})	38.65±15.66	114.29±18.01	73.27±33.32	- [b]
SO_2 (ppb)	1.99±0.45	2.21±0.69	2.18±0.54	0.82±0.42
HCHO (ppb)	1.91±1.05	5.38 ±1.08	3.67±0.68	-
HMS (μg m^{-3})	0.23±0.08	0.36±0.09	0.32±0.08	0.050±0.012
Sulfate (μg m^{-3})	4.18±1.71	11.44±4.07	8.87±4.05	2.09±0.46
HMS/Sulfate (%)	5.87±1.70%	3.36±0.73%	4.15±1.40%	2.57±0.09%
ALWC (μg m^{-3})	22.69±20.65	80.45±38.40	61.30±36.34	14.72±6.40
pH	5.25±0.42	4.76±0.46	3.95±0.53	4.24±0.15
Ionic strength (mol kg^{-1})	12.32±3.19	8.85±1.30	10.39±0.85	4.30±1.24
P_{HMS} (× 10^{-4} μg m^{-3} h^{-1})	4.54±8.4	57.6±58.7	1.18±1.87	0.26 [c]
HMS/CO	0.38±0.14	0.51±0.11	0.35±0.12	-

[a] The numerical representation of average ± one standard deviation.

[b] The data was not available.

[c] The formation rate was calculated using averaged values listed above assuming the HCHO level of 0.5 ppb (Wagner et al., 2001; Anderson et al., 2017).

Table S2. Collection and chemical composition of marine samples.

No.	Collection date and duration [a]	Collection sites [b]	$PM_{2.5}$ samples			SO_2 samples	
			HMS	Sulfate	HMS/Sulfate	SO_2 (ppb)	CE
1	4/13/2024 (960 min)	B01-B02	0.03	2.72	0.012	0.79	0.94
2	4/17/2024 (1083 min)	B17-B23	0.04	1.63	0.024	0.22	0.49
3	4/18/2024 (841 min)	N22-N15	0.06	2.09	0.027	-	-
4	4/23/2024 (1055 min)	H21-H17	0.07	2.07	0.032	1.03	0.97
5	4/24/2024 (1058 min)	H15-H11	0.06	2.47	0.026	0.49	0.61
6	4/25/2024 (961 min)	H9-H3	0.04	2.84	0.016	1.59	0.52

[a] Daily aerosol and gas samples were collected while the sampling duration was not uniform as these samplers were temporarily switched off whenever the boat halted to prevent contamination from fuel emissions.

[b] These collection sites denote the specific locations where the research vessel has passed through on the respective sampling days.

Table S3. Ionic strength (IS) effects on aqueous reaction rate coefficient and equilibrium constants in electrolyte solutions.

Parameter	Expressions	Notes
R_{HMS}	$P_{HMS} = \left\{\frac{1}{K_h+1}\left(\frac{k_1 k_{a1}[H^+] + k_2 k_{a1} k_{a2}}{[H^+]^2}\right)\right\} H_{SO2} P_{SO2} H_{HCHO} P_{HCHO}$	
H_{SO2}	$\log H_{SO2} = \log H_{SO2}^{IS=0} + \left(\frac{22.3}{T} - 0.0997\right) \times IS$ [a], (Millero et al., 1989)	IS_{max} = 6 mol kg^{-1} [b]
$H_{SO2}^{IS=0}$	$H_{SO2}^{IS=0} = 1.23 \times \exp\left(3145.3 \times \left(\frac{1}{T} - \frac{1}{298}\right)\right)$ (Seinfeld and Pandis, 2016)	
H_{HCHO}	$H_{HCHO} = \exp\left(\frac{1641.3}{T} - 3.089\right)$ (Seinfeld and Pandis, 2016)	
K_h	$K_h = \exp\left(\frac{3769}{T} - 5.494\right)$ (Winkelman et al., 2002)	
k_{a1}	$\log k_{a1} = \log k_{a1}^{IS=0} + 0.5 \times \sqrt{IS} - 0.31 \times IS$ [a], (Millero et al., 1989)	IS_{max} = 6 mol kg^{-1} [b]
$k_{a1}^{IS=0}$	$k_{a1}^{IS=0} = 0.013 \times \exp\left(1960 \times \left(\frac{1}{T} - \frac{1}{298}\right)\right)$	
k_{a2}	$\log k_{a2} = \log k_{a2}^{IS=0} + 1.052 \times \sqrt{IS} - 0.36 \times IS$ [a], (Millero et al., 1989)	IS_{max} = 6 mol kg^{-1} [b]
$k_{a2}^{IS=0}$	$k_{a2}^{IS=0} = 6.6 \times 10^{-8} \times \exp\left(1500 \times \left(\frac{1}{T} - \frac{1}{298}\right)\right)$ (Seinfeld and Pandis, 2016)	
k_1	$k_1 = k_1^{IS=0} \times \exp\left(7.12 \times \frac{IS}{0.09+IS} - 0.10\right)/320$ (Zhang et al., 2023)	IS_{max} = 11 mol kg^{-1} [b]
$k_1^{IS=0}$	$k_1^{IS=0} = 3.2 \times 10^2 \times \exp\left(-2700 \times \left(\frac{1}{T} - \frac{1}{298}\right)\right)$ (Boyce et al., 1984)	
k_2	$k_2 = 1.13 \times 10^4 \times k_1$ (Zhang et al., 2023)	IS_{max} = 11 mol kg^{-1}

[a] The expressions were established based on the measured results.

[b] IS_{max} refers to the maximum ionic strength investigated in corresponding laboratory references.

[c] This T-dependent relation was established based on the laboratory results (Zhang et al., 2023), assuming that the ionic strength effect remains the same at the temperature range (268-281 K) observed in this work.

References:

Anderson, D. C., Nicely, J. M., Wolfe, G. M., Hanisco, T. F., Salawitch, R. J., Canty, T. P., Dickerson, R. R., Apel, E. C., Baidar, S., Bannan, T. J., Blake, N. J., Chen, D., Dix, B., Fernandez, R. P., Hall, S. R., Hornbrook, R. S., Gregory Huey, L., Josse, B., Jöckel, P., Kinnison, D. E., Koenig, T. K., Le Breton, M., Marécal, V., Morgenstern, O., Oman, L. D., Pan, L. L., Percival, C., Plummer, D., Revell, L. E., Rozanov, E., Saiz-Lopez, A., Stenke, A., Sudo, K., Tilmes, S., Ullmann, K., Volkamer, R., Weinheimer, A. J. and Zeng, G.: Formaldehyde in the Tropical Western Pacific: Chemical Sources and Sinks, Convective Transport, and Representation in CAM-Chem and the CCMI Models, Journal of Geophysical Research: Atmospheres, 122(20): 11,201-211,226, https://doi.org/10.1002/2016JD026121, 2017.

Battaglia, M. A., Weber, R. J., Nenes, A. and Hennigan, C. J.: Effects of water-soluble organic carbon on aerosol pH, Atmospheric Chemistry and Physics, 19(23): 14607-14620, 10.5194/acp-19-14607-2019, 2019.

Boyce, S. D. and Hoffmann, M. R.: Kinetics and mechanism of the formation of hydroxymethanesulfonic acid at low pH, The Journal of Physical Chemistry, 88(20): 4740-4746, 10.1021/j150664a059, 1984.

Campbell, J. R., Battaglia, M., Jr., Dingilian, K., Cesler-Maloney, M., St Clair, J. M., Hanisco, T. F., Robinson, E., DeCarlo, P., Simpson, W., Nenes, A., Weber, R. J. and Mao, J.: Source and Chemistry of Hydroxymethanesulfonate (HMS) in Fairbanks, Alaska, Environmental Science & Technology, 56(12): 7657-7667, 10.1021/acs.est.2c00410, 2022.

Cheng, Y., Zheng, G., Wei, C., Mu, Q., Zheng, B., Wang, Z., Gao, M., Zhang, Q., He, K., Carmichael, G., Pöschl, U. and Su, H.: Reactive nitrogen chemistry in aerosol water as a source of sulfate during haze events in China, Science Advances, 2(12): e1601530, doi:10.1126/sciadv.1601530, 2016.

Chow, J. C., Watson, J. G., Chen, L. W., Chang, M. C., Robinson, N. F., Trimble, D. and Kohl, S.: The IMPROVE_A temperature protocol for thermal/optical carbon analysis: maintaining consistency with a long-term database, J Air Waste Manag Assoc, 57(9): 1014-1023, 10.3155/1047-3289.57.9.1014, 2007.

De Haan, D. O., Jansen, K., Rynaski, A. D., Sueme, W. R. P., Torkelson, A. K., Czer, E. T., Kim, A. K., Rafla, M. A., De Haan, A. C. and Tolbert, M. A.: Brown Carbon Production by Aqueous-Phase Interactions of Glyoxal and SO_2, Environmental Science & Technology, 54(8): 4781-4789, 10.1021/acs.est.9b07852, 2020.

Ding, J., Zhao, P., Su, J., Dong, Q., Du, X. and Zhang, Y.: Aerosol pH and its driving factors in Beijing, Atmospheric Chemistry and Physics, 19(12): 7939-7954, 10.5194/acp-19-7939-2019, 2019.

Dingilian, K., Hebert, E., Battaglia, M., Jr., Campbell, J. R., Cesler-Maloney, M., Simpson, W., St. Clair, J. M., Dibb, J., Temime-Roussel, B., D'Anna, B., Moon, A., Alexander, B., Yang, Y., Nenes, A., Mao, J. and Weber, R. J.: Hydroxymethanesulfonate and Sulfur(IV) in Fairbanks Winter During the ALPACA Study, ACS ES&T Air, 1(7): 646-659, 10.1021/acsestair.4c00012, 2024.

Dixon, R. W. and Aasen, H.: Measurement of hydroxymethanesulfonate in atmospheric aerosols, Atmospheric Environment, 33(13): 2023-2029, https://doi.org/10.1016/S1352-2310(98)00416-6, 1999.

Fan, M.-Y., Hong, Y., Zhang, Y.-L., Sha, T., Lin, Y.-C., Cao, F. and Guo, H.: Increasing Nonfossil Fuel Contributions to Atmospheric Nitrate in Urban China from Observation to Prediction, Environmental Science & Technology, 57(46): 18172-18182, 10.1021/acs.est.3c01651, 2023.

Fan, M.-Y., Zhang, Y.-L., Lin, Y.-C., Chang, Y.-H., Cao, F., Zhang, W.-Q., Hu, Y.-B., Bao, M.-Y., Liu, X.-Y., Zhai, X.-Y., Lin, X., Zhao, Z.-Y. and Song, W.-H.: Isotope-based source apportionment of nitrogen-containing aerosols: A case study in an industrial city in China, Atmospheric Environment, 212: 96-105, 10.1016/j.atmosenv.2019.05.020, 2019.

Feng, X., Chen, Y., Liu, Z., Feng, Y., Du, H., Mu, Y. and Chen, J.: Exploring the Influence of 34S

Fractionation From Emission Sources and SO$_2$ Atmospheric Oxidation on Sulfate Source Apportionment Based on Hourly Resolution δ^{34}S-SO$_2$/SO$_4^{2-}$, Journal of Geophysical Research: Atmospheres, 128(8): e2023JD038595, https://doi.org/10.1029/2023JD038595, 2023.

Guo, Z., Guo, Q., Chen, S., Zhu, B., Zhang, Y., Yu, J. and Guo, Z.: Study on pollution behavior and sulfate formation during the typical haze event in Nanjing with water soluble inorganic ions and sulfur isotopes, Atmospheric Research, 217: 198-207, https://doi.org/10.1016/j.atmosres.2018.11.009, 2019.

Han, X., Lang, Y., Guo, Q., Li, X., Ding, H. and Li, S.: Enhanced Oxidation of SO$_2$ by H$_2$O$_2$ During Haze Events: Constraints From Sulfur Isotopes, Journal of Geophysical Research: Atmospheres, 127(13): e2022JD036960, https://doi.org/10.1029/2022JD036960, 2022.

Hong, Q., Zhu, L., Xing, C., Hu, Q., Lin, H., Zhang, C., Zhao, C., Liu, T., Su, W. and Liu, C.: Inferring vertical variability and diurnal evolution of O$_3$ formation sensitivity based on the vertical distribution of summertime HCHO and NO$_2$ in Guangzhou, China, Science of Total Environment, 827: 154045, 10.1016/j.scitotenv.2022.154045, 2022a.

Hong, Y., Cao, F., Fan, M.-Y., Lin, Y.-C., Bao, M., Xue, Y., Wu, J., Yu, M., Wu, X. and Zhang, Y.-L.: Using machine learning to quantify sources of light-absorbing water-soluble humic-like substances (HULISws) in Northeast China, Atmospheric Environment, 291: 119371, https://doi.org/10.1016/j.atmosenv.2022.119371, 2022b.

Lai, D., Wong, Y. K., Xu, R., Xing, S., Ng, S. I. M., Kong, L., Yu, J. Z., Huang, D. D. and Chan, M. N.: Significant Conversion of Organic Sulfur from Hydroxymethanesulfonate to Inorganic Sulfate and Peroxydisulfate Ions upon Heterogeneous OH Oxidation, Environmental Science & Technology Letters, 10(9): 773-778, 10.1021/acs.estlett.3c00472, 2023.

Li, J., Hua, C., Ma, L., Chen, K., Zheng, F., Chen, Q., Bao, X., Sun, J., Xie, R., Bianchi, F., Kerminen, V.-M., Petäjä, T., Kulmala, M. and Liu, Y.: Key drivers of the oxidative potential of PM2.5 in Beijing in the context of air quality improvement from 2018 to 2022, Environment International, 187: 108724, https://doi.org/10.1016/j.envint.2024.108724, 2024.

Liu, C., Xing, C., Hu, Q., Li, Q., Liu, H., Hong, Q., Tan, W., Ji, X., Lin, H., Lu, C., Lin, J., Liu, H., Wei, S., Chen, J., Yang, K., Wang, S., Liu, T. and Chen, Y.: Ground-Based Hyperspectral Stereoscopic Remote Sensing Network: A Promising Strategy to Learn Coordinated Control of O$_3$ and PM$_{2.5}$ over China, Engineering, 19: 71-83, 10.1016/j.eng.2021.02.019, 2022.

Liu, J., Zhang, F., Xu, W., Sun, Y., Chen, L., Li, S., Ren, J., Hu, B., Wu, H. and Zhang, R.: Hygroscopicity of Organic Aerosols Linked to Formation Mechanisms, Geophysical Research Letters, 48(4): e2020GL091683, https://doi.org/10.1029/2020GL091683, 2021a.

Liu, T., Chan, A. W. H. and Abbatt, J. P. D.: Multiphase Oxidation of Sulfur Dioxide in Aerosol Particles: Implications for Sulfate Formation in Polluted Environments, Environmental Science & Technology, 55(8): 4227-4242, 10.1021/acs.est.0c06496, 2021b.

Ma, T., Furutani, H., Duan, F., Kimoto, T., Jiang, J., Zhang, Q., Xu, X., Wang, Y., Gao, J., Geng, G., Li, M., Song, S., Ma, Y., Che, F., Wang, J., Zhu, L., Huang, T., Toyoda, M. and He, K.: Contribution of hydroxymethanesulfonate (HMS) to severe winter haze in the North China Plain, Atmospheric Chemistry and Physics, 20(10): 5887-5897, 10.5194/acp-20-5887-2020, 2020.

Millero, F. J., Hershey, J. P., Johnson, G. and Zhang, J.-Z.: The solubility of SO$_2$ and the dissociation of H$_2$SO$_3$ in NaCl solutions, Journal of Atmospheric Chemistry, 8(4): 377-389, 10.1007/bf00052711, 1989.

Moch, J. M., Dovrou, E., Mickley, L. J., Keutsch, F. N., Cheng, Y., Jacob, D. J., Jiang, J., Li, M., Munger, J. W., Qiao, X. and Zhang, Q.: Contribution of Hydroxymethane Sulfonate to Ambient Particulate Matter: A Potential Explanation for High Particulate Sulfur During Severe Winter Haze in Beijing, Geophysical

Research Letters, 45(21), 10.1029/2018gl079309, 2018.

Moch, J. M., Dovrou, E., Mickley, L. J., Keutsch, F. N., Liu, Z., Wang, Y., Dombek, T. L., Kuwata, M., Budisulistiorini, S. H., Yang, L., Decesari, S., Paglione, M., Alexander, B., Shao, J., Munger, J. W. and Jacob, D. J.: Global Importance of Hydroxymethanesulfonate in Ambient Particulate Matter: Implications for Air Quality, J Geophys Res Atmos, 125(18): e2020JD032706, 10.1029/2020JD032706, 2020.

Munger, J. W., Tiller, C. and Hoffmann, M. R.: Identification of Hydroxymethanesulfonate in Fog Water, Science, 231(4735): 247-249, doi:10.1126/science.231.4735.247, 1986.

Olson, T. M. and Hoffmann, M. R.: On the kinetics of formaldehyde-S(IV) adduct formation in slightly acidic solution, Atmospheric Environment (1967), 20(11): 2277-2278, https://doi.org/10.1016/0004-6981(86)90318-5, 1986.

Petters, M. D. and Kreidenweis, S. M.: A single parameter representation of hygroscopic growth and cloud condensation nucleus activity, Atmos. Chem. Phys., 7(8): 1961-1971, 10.5194/acp-7-1961-2007, 2007.

Pöhlker, M. L., Pöhlker, C., Quaas, J., Mülmenstädt, J., Pozzer, A., Andreae, M. O., Artaxo, P., Block, K., Coe, H., Ervens, B., Gallimore, P., Gaston, C. J., Gunthe, S. S., Henning, S., Herrmann, H., Krüger, O. O., McFiggans, G., Poulain, L., Raj, S. S., Reyes-Villegas, E., Royer, H. M., Walter, D., Wang, Y. and Pöschl, U.: Global organic and inorganic aerosol hygroscopicity and its effect on radiative forcing, Nature Communications, 14(1): 6139, 10.1038/s41467-023-41695-8, 2023.

Rodgers, C. D.: Inverse methods for atmospheric sounding: theory and practice, World scientific, ISBN 9814498688, 2000.

Seinfeld, J. and Pandis, S.: Atmospheric chemistry and physics: from air pollution to climate change, Wiley, ISBN 978-1-119-22117-3, 2016.

Song, S., Gao, M., Xu, W., Shao, J., Shi, G., Wang, S., Wang, Y., Sun, Y. and McElroy, M. B.: Fine-particle pH for Beijing winter haze as inferred from different thermodynamic equilibrium models, Atmospheric Chemistry and Physics, 18(10): 7423-7438, 10.5194/acp-18-7423-2018, 2018.

Spurr, R. J. D.: VLIDORT: A linearized pseudo-spherical vector discrete ordinate radiative transfer code for forward model and retrieval studies in multilayer multiple scattering media, Journal of Quantitative Spectroscopy and Radiative Transfer, 102(2): 316-342, https://doi.org/10.1016/j.jqsrt.2006.05.005, 2006.

Stelson, A. W. and Seinfeld, J. H.: Chemical mass accounting of urban aerosol, Environmental Science & Technology, 15(6): 671-679, 10.1021/es00088a005, 1981.

Wagner, V., Schiller, C. and Fischer, H.: Formaldehyde measurements in the marine boundary layer of the Indian Ocean during the 1999 INDOEX cruise of the R/V Ronald H. Brown, Journal of Geophysical Research: Atmospheres, 106(D22): 28529-28538, 10.1029/2000jd900825, 2001.

Wang, H., Li, J., Wu, T., Ma, T., Wei, L., Zhang, H., Yang, X., Munger, J. W., Duan, F. K., Zhang, Y., Feng, Y., Zhang, Q., Sun, Y., Fu, P., McElroy, M. B. and Song, S.: Model Simulations and Predictions of Hydroxymethanesulfonate (HMS) in the Beijing-Tianjin-Hebei Region, China: Roles of Aqueous Aerosols and Atmospheric Acidity, Environ Sci Technol, 58(3): 1589-1600, 10.1021/acs.est.3c07306, 2024.

Wei, L., Fu, P., Chen, X., An, N., Yue, S., Ren, H., Zhao, W., Xie, Q., Sun, Y., Zhu, Q.-F., Wang, Z. and Feng, Y.-Q.: Quantitative Determination of Hydroxymethanesulfonate (HMS) Using Ion Chromatography and UHPLC-LTQ-Orbitrap Mass Spectrometry: A Missing Source of Sulfur during Haze Episodes in Beijing, Environmental Science & Technology Letters, 7(10): 701-707, 10.1021/acs.estlett.0c00528, 2020.

Winkelman, J. G. M., Voorwinde, O. K., Ottens, M., Beenackers, A. A. C. M. and Janssen, L. P. B. M.: Kinetics and chemical equilibrium of the hydration of formaldehyde, Chemical Engineering Science, 57(19): 4067-4076, https://doi.org/10.1016/S0009-2509(02)00358-5, 2002.

Wu, X., Sun, W., Huai, B., Wang, L., Han, C., Wang, Y. and Mi, W.: Seasonal variation and sources of atmospheric polycyclic aromatic hydrocarbons in a background site on the Tibetan Plateau, Journal of Environmental Sciences, 125: 524-532, https://doi.org/10.1016/j.jes.2022.02.042, 2023.

Xing, C., Liu, C., Wang, S., Chan, K. L., Gao, Y., Huang, X., Su, W., Zhang, C., Dong, Y., Fan, G., Zhang, T., Chen, Z., Hu, Q., Su, H., Xie, Z. and Liu, J.: Observations of the vertical distributions of summertime atmospheric pollutants and the corresponding ozone production in Shanghai, China, Atmospheric Chemistry and Physics, 17(23): 14275-14289, 10.5194/acp-17-14275-2017, 2017.

Xing, C., Liu, C., Wu, H., Lin, J., Wang, F., Wang, S. and Gao, M.: Ground-based vertical profile observations of atmospheric composition on the Tibetan Plateau (2017–2019), Earth System Science Data, 13(10): 4897-4912, 10.5194/essd-13-4897-2021, 2021.

Yu, C., Liu, T., Ge, D., Nie, W., Chi, X. and Ding, A.: Ionic Strength Enhances the Multiphase Oxidation Rate of Sulfur Dioxide by Ozone in Aqueous Aerosols: Implications for Sulfate Production in the Marine Atmosphere, Environ Sci Technol, 57(16): 6609-6615, 10.1021/acs.est.3c00212, 2023.

Zhang, H., Xu, Y. and Jia, L.: Hydroxymethanesulfonate formation as a significant pathway of transformation of SO_2, Atmospheric Environment, 294, 10.1016/j.atmosenv.2022.119474, 2023.

Zhang, Y., Han, R., Sun, X., Sun, C., Griffith, S. M., Wu, G., Li, L., Li, W., Zhao, Y., Li, M., Zhou, Z., Wang, W., Sheng, L., Yu, J. Z. and Zhou, Y.: Sulfate Formation Driven by Wintertime Fog Processing and a Hydroxymethanesulfonate Complex With Iron: Observations From Single-Particle Measurements in Hong Kong, Journal of Geophysical Research: Atmospheres, 129(12), 10.1029/2023jd040512, 2024.

Zhang, Y., Liu, Y., Ma, W., Hua, C., Zheng, F., Lian, C., Wang, W., Xia, M., Zhao, Z., Li, J., Xie, J., Wang, Z., Wang, Y., Chen, X., Zhang, Y., Feng, Z., Yan, C., Chu, B., Du, W., Kerminen, V.-M., Bianchi, F., Petäjä, T., Worsnop, D. and Kulmala, M.: Changing aerosol chemistry is redefining HONO sources, Nature Communications, 16(1), 10.1038/s41467-025-60614-7, 2025.